the source-drain voltage relative to the back-gate voltage (*11*).

In our TI-FMI heterostructure, the drop of μ across the magnetic structure was small compared with the drop of μ across source and drain (due to the ratio of their lengths), and therefore the local μ determined the magnitude of the chiral edge current. Because current magnetometry is a lock-in measurement (*31*), the measured magnetic response from the chiral current is proportional to the modulation of the local μ when the Fermi level is in the surface gap. When the domain boundary is close to the alternating AC voltage bias (Fig. 4, B and G), μ is more strongly modulated than when it is close to the ground (Fig. 4, C and F), yielding a stronger chiral current intensity in current magnetometry (Fig. 4H). The magnitude of the extracted current I (fig. S5B) along the magnetic domain boundary (*31*) is in agreement with calculations of the current carried by one spin-polarized edge mode in the ballistic transport regime $I = e\mu/h$ (*11*, *35*, *36*).

Our results not only demonstrate the existence of CES at the magnetic domain boundary of a TI but also establish a versatile platform in scanning SQUID microscopy for imaging and manipulating broken TRS TI surface states on the mesoscopic scale. The broken TRS state and its chiral edge will be a playground for exploring interaction between TIs and FMIs (*37*–*40*).

REFERENCES AND NOTES

1. X.-L. Qi, S.-C. Zhang, *Rev. Mod. Phys.* **83**, 1057–1110 (2011).
2. M. Z. Hasan, C. L. Kane, *Rev. Mod. Phys.* **82**, 3045–3067 (2010).
3. Y. H. Wang, H. Steinberg, P. Jarillo-Herrero, N. Gedik, *Science* **342**, 453–457 (2013).
4. O. Pankratov, *Phys. Lett. A* **121**, 360–366 (1987).
5. A. Y. Kitaev, *Physics-Uspekhi* **44** (10S), 131–136 (2001).
6. L. Fu, C. L. Kane, *Phys. Rev. Lett.* **100**, 096407 (2008).
7. A. R. Akhmerov, J. Nilsson, C. W. Beenakker, *Phys. Rev. Lett.* **102**, 216404 (2009).
8. C. Z. Chang *et al.*, *Science* **340**, 167–170 (2013).
9. X. Kou *et al.*, *Phys. Rev. Lett.* **113**, 137201 (2014).
10. R. Yu *et al.*, *Science* **329**, 61–64 (2010).
11. S. Datta, *Electronic Transport in Mesoscopic Systems* (Cambridge Univ. Press, Cambridge, 1995).
12. Q. Meng, S. Vishveshwara, T. L. Hughes, *Phys. Rev. Lett.* **109**, 176803 (2012).
13. C. Wickles, W. Belzig, *Phys. Rev. B* **86**, 035151 (2012).
14. T. Yokoyama, S. Murakami, *Physica E* (2013).
15. G. J. Ferreira, D. Loss, *Phys. Rev. Lett.* **111**, 106802 (2013).
16. P. Wei *et al.*, *Phys. Rev. Lett.* **110**, 186807 (2013).
17. J. S. Moodera, X. Hao, G. A. Gibson, R. Meservey, *Phys. Rev. Lett.* **61**, 637–640 (1988).
18. D. Ghosh, M. De, S. K. De, *Phys. Rev. B* **70**, 115211 (2004).
19. D. O'Mahony *et al.*, *Thin Solid Films* **488**, 200–203 (2005).
20. Y. Xia *et al.*, *Nat. Phys.* **5**, 398–402 (2009).
21. Y. Zhang *et al.*, *Nat. Phys.* **6**, 584 (2010).
22. J. G. Analytis *et al.*, *Nat. Phys.* **6**, 960–964 (2010).
23. Y. H. Wang *et al.*, *Phys. Rev. Lett.* **107**, 207602 (2011).
24. Q. I. Yang *et al.*, *Phys. Rev. B* **88**, 081407 (2013).
25. K. C. Nowack *et al.*, *Nat. Mater.* **12**, 787–791 (2013).
26. E. M. Spanton *et al.*, *Phys. Rev. Lett.* **113**, 026804 (2014).
27. B. W. Gardner *et al.*, *Rev. Sci. Instrum.* **72**, 2361 (2001).
28. J. R. Kirtley *et al.*, Advanced sensors for scanning SQUID microscopy, *Proceedings of the 14th International Superconducting Electronics Conference (ISEC)*, 2013.
29. M. E. Huber *et al.*, *IEEE Trans. Appl. Supercond.* **11**, 4048–4053 (2001).
30. It is possible to induce CES with in-plane magnetization, but the effect may be very weak in Bi_2Se_3 (*41*) because of the small warping effect (*23*).
31. See the supplementary materials on *Science* Online.
32. A. Zyuzin, A. Burkov, *Phys. Rev. B* **83**, 195413 (2011).
33. J. G. Checkelsky, Y. S. Hor, R. J. Cava, N. P. Ong, *Phys. Rev. Lett.* **106**, 196801 (2011).
34. D. Yoshioka, *The Quantum Hall Effect* (Springer, Berlin, 2002)
35. A. T. Lee, M. J. Han, K. Park, *Phys. Rev. B* **90**, 155103 (2014).
36. V. Men'shov, V. Tugushev, S. Eremeev, P. Echenique, E. Chulkov, *Phys. Rev. B* **88**, 224401 (2013).
37. J. Checkelsky, J. T. Ye, Y. Onose, Y. Iwasa, Y. Tokura, *Nat. Phys.* **8**, 729–733 (2012).
38. Y. Tserkovnyak, D. Loss, *Phys. Rev. Lett.* **108**, 187201 (2012).
39. A. R. Mellnik *et al.*, *Nature* **511**, 449–451 (2014).
40. R. Hammer, W. Potz, *Phys. Rev. B* **88**, 235119 (2013).
41. C.-X. Liu *et al.*, *Phys. Rev. B* **81**, 041307 (2010).

ACKNOWLEDGMENTS

These measurements were supported by the Center for Function Accelerated nanoMaterial Engineering (FAME), one of six centers of STARnet, a Semiconductor Research Corporation program sponsored by the Microelectronics Advanced Research Corp. (MARCO) and the Defense Advanced Research Projects Agency (DARPA). Preliminary measurements and analysis were supported by the Department of Energy (DOE), Office of Science, Basic Energy Sciences, Materials Sciences and Engineering Division, under contract DE-AC02-76SF00515. The SQUID microscope and sensors were developed with support from NSF-NSEC 0830228 and NSF IMR-MIP 0957616. Y.H.W. is partially supported by the Urbanek Fellowship of the Department of Applied Physics at Stanford University. For sample preparation, F.K., P.J-H., and J.S.M. acknowledge support by the Massachusetts Institute of Technology's Materials Research Science and Engineering Center (MRSEC) through the MRSEC Program of the National Science Foundation under award DMR-0819762. Partial support for sample development was provided by NSF (DMR-1207469), ONR (N00014-13-1-0301) (F.K. and J.S.M.), and by the DOE, Basic Energy Sciences Office, Division of Materials Sciences and Engineering, under award no. DE-SC0006418 (F.K. and P.J-H.). We are grateful for the assistance from G. Gibson, M. Ketchen, and M. Huber on developing the SQUID sensors and from I. Sochnikov, E. Spanton, J. Palmstrom, and K. C. Nowack on the measurement, as well as for stimulating discussions with S.-C. Zhang, X.-L. Qi, J. Wang, D. Goldhaber-Gordon, and B. I. Halperin.

SUPPLEMENTARY MATERIALS

www.sciencemag.org/content/349/6251/948/suppl/DC1
Materials and Methods
Supplementary Text
Figs. S1 to S12
Reference (*42*)

21 October 2014; accepted 29 July 2015
Published online 13 August 2015
10.1126/science.aaa0508

QUANTUM MECHANICS

Quantum squeezing of motion in a mechanical resonator

E. E. Wollman,[1]* C. U. Lei,[1]* A. J. Weinstein,[1]* J. Suh,[2] A. Kronwald,[3] F. Marquardt,[3,4] A. A. Clerk,[5] K. C. Schwab[1]†

According to quantum mechanics, a harmonic oscillator can never be completely at rest. Even in the ground state, its position will always have fluctuations, called the zero-point motion. Although the zero-point fluctuations are unavoidable, they can be manipulated. Using microwave frequency radiation pressure, we have manipulated the thermal fluctuations of a micrometer-scale mechanical resonator to produce a stationary quadrature-squeezed state with a minimum variance of 0.80 times that of the ground state. We also performed phase-sensitive, back-action evading measurements of a thermal state squeezed to 1.09 times the zero-point level. Our results are relevant to the quantum engineering of states of matter at large length scales, the study of decoherence of large quantum systems, and for the realization of ultrasensitive sensing of force and motion.

In the quantum ground state, a mechanical resonator has position fluctuations divided equally between its two motional quadratures, $\hat{X}_1$ and $\hat{X}_2$, which are defined as the slowly varying envelopes of the position: $\hat{x} = \hat{X}_1\cos(\omega_m t) + \hat{X}_2\sin(\omega_m t)$. Additionally, the ground-state fluctuations minimize the uncertainty relation given by the quadratures' nonzero commutator: $\langle\Delta\hat{X}_1^2\rangle\langle\Delta\hat{X}_2^2\rangle \geq \frac{1}{4}|\langle[\hat{X}_1,\hat{X}_2]\rangle|^2 = x_{zp}^4$, where $x_{zp} = \sqrt{\hbar/2m\omega_m}$ is the amplitude of the zero-point fluctuations. Given this uncertainty relation, it is, in principle, possible to squeeze the zero-point noise such that fluctuations in one quadrature are reduced below the zero-point level at the expense of increasing noise in the orthogonal quadrature. More generally, other noncommuting observable pairs can be squeezed, and squeezed states have been created and detected in such varied systems as optical (*1*) and microwave (*2*) modes, the motion of trapped ions (*3*), and spin states in an ensemble of cold atoms (*4*). Transient quantum squeezing has also been created and observed in the motion of molecular nuclei (*5*) and of terahertz-frequency phonons in an atomic lattice on picosecond time scales (*6*). Here, we demonstrate steady-state squeezing of a micrometer-scale mechanical resonator by implementing a reservoir-engineering scheme (*7*) that is closely

[1]Applied Physics, California Institute of Technology, Pasadena, CA 91125, USA. [2]Korea Research Institute of Standards and Science, Daejeon 305-340, Republic of Korea. [3]Friedrich-Alexander-Universität Erlangen-Nürnberg, Staudtstraße 7, D-91058 Erlangen, Germany. [4]Max Planck Institute for the Science of Light, Günther-Scharowsky-Straße 1/Bau 24, D-91058 Erlangen, Germany. [5]Department of Physics, McGill University, Montreal, Quebec, H3A 2T8, Canada.
*These authors contributed equally to this work. †Corresponding author. E-mail: schwab@caltech.edu

related to the approach recently used to produce quantum squeezed states in the motion of trapped ions (*8*).

A major challenge for quantum squeezing of a radio-frequency mechanical mode is that, even at a temperature of 10 mK, the thermal occupation and corresponding position fluctuations are far larger than the quantum zero-point fluctuations. $\Delta\hat{x}^2$ is approximately 100 times x_{zp}^2 for a 4 MHz resonator; quantum squeezing can only be accomplished by first overcoming this large thermal contribution. In contrast, optical modes are found in the quantum ground state at room temperature. Squeezing of mechanical fluctuations was first demonstrated far outside the quantum regime by parametrically modulating the mechanical spring constant (*9*). Because parametric methods are limited to 3 dB of steady-state squeezing, the occupation factor of the mechanical mode must be well below one phonon to achieve squeezing below the zero-point fluctuations. There are many theoretical proposals for surpassing the 3-dB limit to produce quantum squeezing via coupling to a qubit (*10*), measurement plus feedback (*11*), injection of squeezed light (*12*), or strong optical pulses (*13*). Experimentally, improvement over the 3-dB limit has been realized with modified parametric techniques (*14*–*16*). Squeezing below the zero-point fluctuations, however, has been an outstanding problem.

Squeezing via reservoir engineering (*7*, *17*) has advantages over other methods, because it creates a system in which the mechanics relaxes into a steady-state squeezed state without the fast measurements and control necessary for feedback. The scheme consists of applying two pump tones to an optical or microwave cavity parametrically coupled to a mechanical resonator. The pumps are detuned from the cavity frequency ω_c by the mechanical frequency $\pm\omega_m$, with the red-detuned pump at a higher power than the blue-detuned pump (Fig. 1A). This is a similar set-up to one used for a back-action evading (BAE) measurement of a single quadrature (*18*), but with excess red-detuned power. The squeezing effect of the drives can be understood as a damping of both quadratures by the excess red-detuned power, similar to that of sideband cooling (*19*), but with less back-action noise added to $\hat{X}_1$ than the zero-point noise associated with the damping. By optimizing the pump power ratio, it is possible to produce arbitrarily large amounts of subzero-point squeezing (i.e., >3 dB) if the coupling between the mechanics and the squeezed reservoir sufficiently dominates the mechanical dissipation rate (*7*).

The effects of both damping and back-action on the amount of squeezing can be seen in the equations for the quadrature fluctuations of the system described above. Here, we take the cavity (mechanics) to be coupled to a bath with thermal occupation n_c^{th} (n_m^{th}) at a rate κ (γ_m). For optical systems, n_c^{th} is usually indistinguishable from 0, but for microwave systems, a nonzero n_c^{th} is commonly observed at high pump powers (*20*, *21*). The presence of the pumps at $\omega_\pm = \omega_c \pm \omega_m$ generates coherent intracavity photon occupations $n_p^\pm$, which are proportional to both the pump power applied at the input of the system and the pump power measured at the output of the measurement chain. The cavity and mechanics are coupled at a single-photon coupling rate $g_0 = \frac{d\omega_c}{dx} x_{zp}$. We also define the enhanced optomechanical coupling rates for the blue and red pumps as $G_\pm = g_0\sqrt{n_p^\pm}$ and the effective optomechanical coupling rate as $\mathcal{G} = \sqrt{G_-^2 - G_+^2}$.

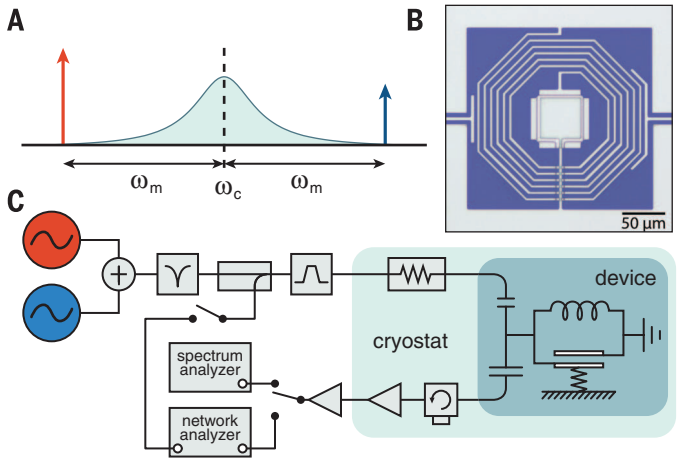

Fig. 1. Measurement setup and device. (**A**) Schematic showing frequencies of squeezing drive tones relative to the cavity frequency. (**B**) Optical micrograph of a typical device. Gray regions are aluminum, and blue regions are the exposed silicon substrate. The center square is a parallel-plate capacitor with a top plate that has a mechanical degree of freedom. The capacitor is surrounded by a spiral inductor, and coupling capacitors on the left and right provide input and output coupling to the device. (**C**) Microwave circuit diagram for squeezing measurements. The red- and blue-detuned tones are filtered at room temperature and attenuated at low temperatures so that they are shot-noise limited at the device. The device is thermally connected to the mixing plate of a dilution refrigerator. Signals are amplified and then measured with a spectrum analyzer or network analyzer.

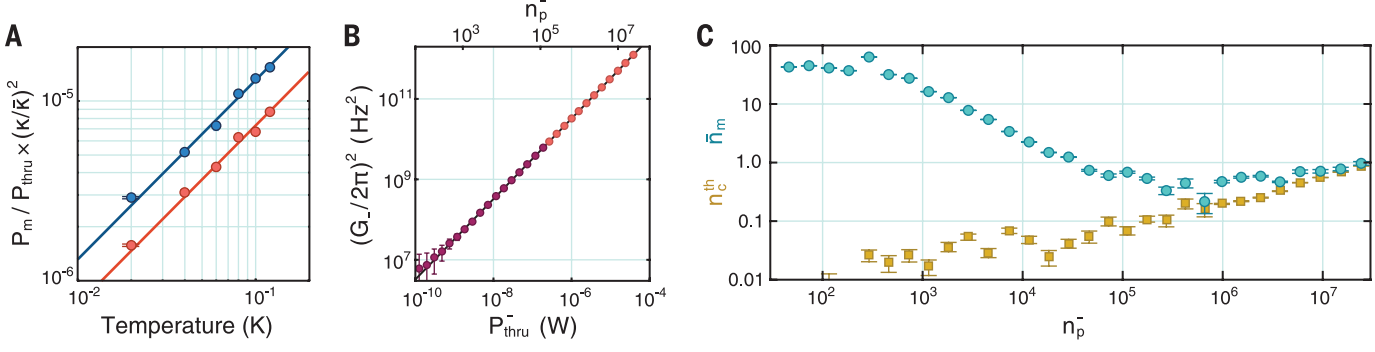

Fig. 2. Calibrations and characterization. (**A**) We measure the integrated mechanical sideband power (P_m) of a weak red-detuned (red) or blue-detuned (blue) pump and normalize by the measured pump power (P_{thru}). This ratio is proportional to the thermal occupation of the mechanics times g_0^2. The difference in slopes is due to the difference in microwave transmission at ω_- and ω_+. (**B**) Enhanced coupling rate calibration for a red-detuned drive. Purple circles, weak-driving regime in which the mechanical susceptibility is a simple Lorentzian; black line, fit to the weak-driving regime damping versus power; red circles, strong-driving regime in which the mechanical linewidth becomes comparable to the cavity linewidth and G_- must be extracted using a full model. (**C**) Characterization of sideband cooling in the presence of a red-detuned drive. Turquoise circles, cooled mechanical occupation; yellow squares, cavity thermal occupation. The mechanical occupation is limited by heating of the cavity bath.

The linearized interaction Hamiltonian for this system is given by

$$\hat{H} = -\hbar\hat{d}^{\dagger}(G_{+}\hat{b}^{\dagger} + G_{-}\hat{b} + G_{+}\hat{b}e^{-2i\omega_m t} + G_{-}\hat{b}^{\dagger}e^{2i\omega_m t}) + \text{H.c.} \quad (1)$$

where $\hat{d}^{\dagger}$ is the cavity photon creation operator and $\hat{b}^{\dagger}$ is the mechanical phonon creation operator. In the good-cavity limit ($\omega_m \gg \kappa$), and when $\kappa \gg \gamma_m$, the quadrature fluctuations are then given by

$$\langle \Delta\hat{X}_{1,2}^2 \rangle = x_{zp}^2 \left\{ \frac{\gamma_m}{\kappa} \frac{(4\mathcal{G}^2 + \kappa^2)}{(4\mathcal{G}^2 + \gamma_m\kappa)} (2n_m^{th} + 1) + \frac{4(G_{-} \mp G_{+})^2}{(4\mathcal{G}^2 + \gamma_m\kappa)} (2n_c^{th} + 1) \right\} \quad (2)$$

For both $\langle \Delta\hat{X}_1^2 \rangle$ and $\langle \Delta\hat{X}_2^2 \rangle$, the first term is proportional to $2n_m^{th} + 1$ and has a prefactor that is less than 1 for all $\mathcal{G} > 0$. This term represents the damping of both quadratures due to the excess red-detuned power. The second term is proportional to $2n_c^{th} + 1$ and is due to the back-action from the microwave field. We see that the back-action is reduced for $\langle \Delta\hat{X}_1^2 \rangle$ and increased for $\langle \Delta\hat{X}_2^2 \rangle$ relative to $\frac{4\mathcal{G}^2}{(4\mathcal{G}^2 + \gamma_m\kappa)}(2n_c^{th} + 1)$, the amount of back-action we would normally associate with the net damping rate set by $\mathcal{G}$. This reduction for $\hat{X}_1$ makes it possible to reduce $\langle \Delta\hat{X}_1^2 \rangle$ below x_{zp}^2.

It is important to note that the quadrature variances depend on the thermal occupations of both the mechanical and cavity baths, which can both be heated by the applied pump power. These thermal occupations are also evident in the noise spectrum of photons leaving the cavity. For our two-port device measured in transmission, the output spectrum derived from the Hamiltonian in Eq. 1 has the form

$$\bar{S}_{VV}[\omega] = S_0 + \kappa_{out}\kappa \frac{(\gamma_m/2)^2 + (\omega - \omega_c)^2}{|f[\omega - \omega_c]|^2} n_c^{th} + \kappa_{out}\gamma_m \frac{G_{-}^2 n_m^{th} + G_{+}^2 (n_m^{th} + 1)}{|f[\omega - \omega_c]|^2} \quad (3)$$

where $f[\omega] = \mathcal{G}^2 + (\gamma_m/2 - i\omega)(\kappa/2 - i\omega)$, κ_{out} is the coupling through the output port of our device, and S_0 is the noise floor of our measurement system. To determine the state of the mechanics, we follow an approach analogous to that used for mechanical cooling measurements in the presence of heated baths (*22*): We fit the output noise spectrum in the presence of the squeezing tones to extract the bath occupations and then infer the quadrature variances for a mechanical resonator coupled to these baths.

Our device consists of a mechanical resonator of frequency $\omega_m = 2\pi \times 3.6$ MHz coupled capacitively to a microwave lumped-element resonator with frequency $\omega_c = 2\pi \times 6.23$ GHz, similar to the device used in (*22*) (Fig. 1B). The bare mechanical linewidth is $\gamma_m = 2\pi \times 3$ Hz at 10 mK, and the cavity linewidth is $\kappa = 2\pi \times 450$ kHz. The optomechanical coupling rate is $g_0 = 2\pi \times 36$ Hz, and the zero-point fluctuations have an amplitude of $x_{zp} \sim 2.3$ fm. Our measurement setup is shown in Fig. 1C. Either we can measure the output noise spectrum of the system (spectral response) or we can sweep a small probe tone through the cavity to measure the complex transmission (driven response). We first calibrate the normalized spectral power at the output of our system using known thermal occupations to find g_0 (Fig. 2A). We then cool our sample temperature to 10 mK, giving an initial thermal occupation of $n_m^{th} \sim 50$ quanta. We calibrate the enhanced optomechanical coupling rate, G_{-}, to the output power of a red-detuned pump by measuring the total mechanical linewidth, $\gamma_{tot} = \gamma_m + 4G_{-}^2/\kappa$, from the driven response of the mechanics for linewidths much smaller than κ (Fig. 2B). As we increase the pump power further, the mechanical linewidth becomes comparable to the cavity bandwidth, and a strong-coupling model of the system is needed to fit the driven response. Fits with this model are in excellent agreement to the low-power calibrations, so we see that the device is well behaved and performs linearly over a broad range of pump powers (Fig. 2B). This agreement also confirms that the dynamics of our system are well described by the linearized Hamiltonian in Eq. 1 in the limit of no blue-detuned power. As we increase the red-detuned pump power, the mechanics becomes more strongly coupled to the cold cavity bath, reaching a minimum occupation of 0.22 ± 0.08 quanta (Fig. 2C). The blue-detuned coupling rate, G_{+}, is also calibrated to the measured

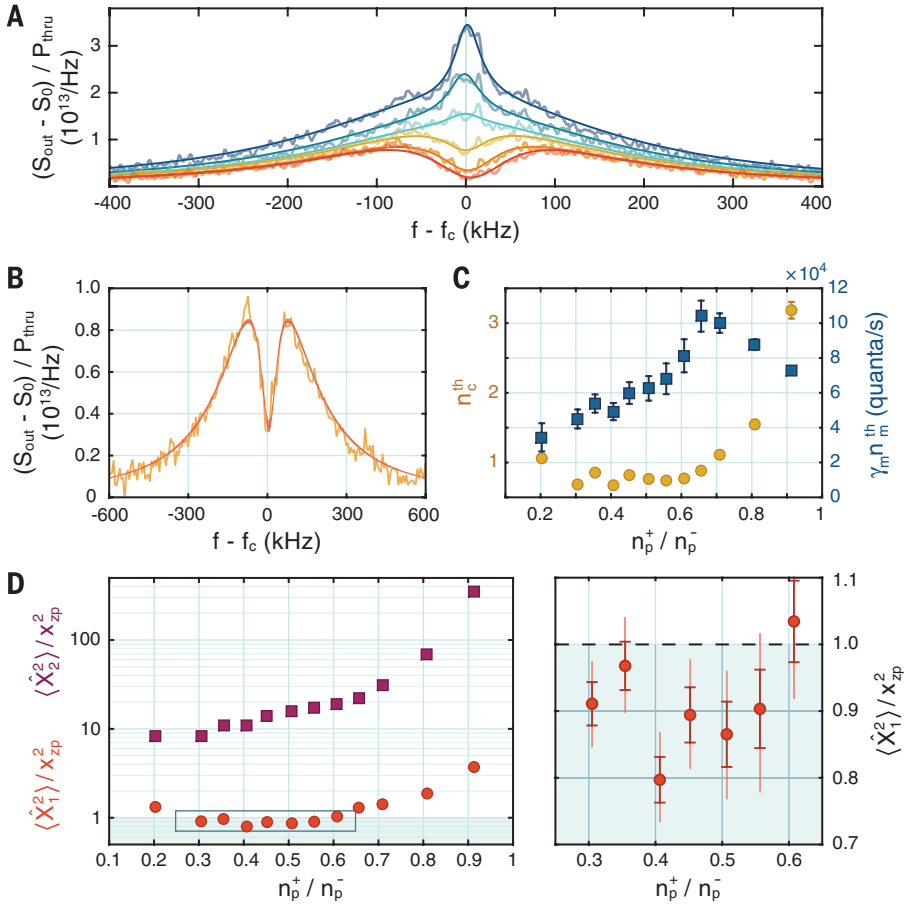

Fig. 3. Squeezing measurements. (**A**) Background-subtracted output spectra normalized by the measured red-detuned pump power at blue/red pump power ratios of 0.3, 0.4, 0.5, 0.6, 0.65, and 0.7, from red to blue. Darker lines indicate fits. All spectra are taken at the total power of $n_p^- + n_p^+ = 1.76 \times 10^7$. As the ratio decreases, the damping increases, broadening the mechanical linewidth and causing the mechanical noise to go from a peak to a dip due to noise squashing. (**B**) Close-up of spectrum and fit at $n_p^+/n_p^- = 0.4$. The thickness of the fit line corresponds to the 95% confidence bounds on the fit. (**C**) Values of n_c^{th} (yellow circles) and $\gamma_m n_m^{th}$ (blue squares) obtained from Bayesian analysis of the spectra. (**D**) (Left) Calculated quadrature noise for $\langle \Delta\hat{X}_1^2 \rangle$ (red circles) and $\langle \Delta\hat{X}_2^2 \rangle$ (purple squares). The shaded region indicates subzero-point squeezing. (Right) Close-up of the boxed area showing data with $\hat{X}_1$ fluctuations below the zero-point level. Dark and light red error bars represent the standard deviation and 95% confidence intervals, respectively. The lowest point has $\langle \Delta\hat{X}_1^2 \rangle / x_{zp}^2 = 0.797 \pm 0.034$. The fit for this point is shown in (B).

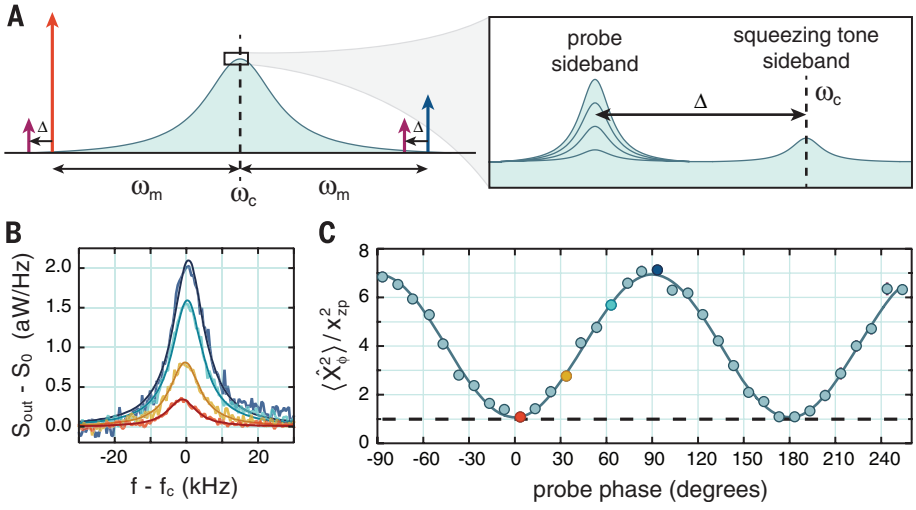

Fig. 4. BAE measurement of squeezing. (**A**) Schematic of pump and probe tone configuration, showing the sideband spectra for different probe phases. (**B**) Measured BAE probe sideband spectra for different probe phases with $n_p^- = 16 \times 10^6$, $n_p^- = 3.2 \times 10^6$, and each $n_p^{probe} = 0.95 \times 10^6$. (**C**) Quadrature variance as a function of phase, as obtained from the calibrated sideband area. The spectra shown in (B) are highlighted in their corresponding color. The zero-point variance is indicated with a dashed black line.

output power using the G_- calibration and a measurement of the output gain at ω_+ versus ω_- (*23*).

To squeeze the mechanical motion, a red-detuned pump is applied at $\omega_c - \omega_m$ and a weaker, blue-detuned pump is applied at $\omega_c + \omega_m$, such that their sidebands overlap at the cavity frequency, as described above. We then measure the output spectrum in the lab frame at different pump power ratios and fit a spectral model to the background-subtracted output spectrum normalized by the measured pump power (Fig. 3A). The spectral model includes "bad-cavity" effects that arise when $\omega_m \not\gg \kappa$ and does not assume that the pumps are aligned at precisely $\omega_c \pm \omega_m$. For our device, the former correction is small, because $\kappa/\omega_m \sim 0.1$. In the absence of these effects, the model reduces to Eq. 3. Because we determine G_- and G_+ from our calibrations and measure κ to high precision with a driven response, the only unknown parameters are n_c^{th} and $\gamma_m n_m^{th}$. For parameter estimation, we use a Bayesian analysis that systematically incorporates both the uncertainty from nonlinear fitting and the uncertainty in the independent calibration measurements. Given the observed data and our knowledge of the system Hamiltonian, we directly sample the posterior probability distribution of all system parameters. We then use this distribution to extract estimators for the bath occupations, n_c^{th} and $\gamma_m n_m^{th}$, and for the mechanical quadrature occupations $\langle \Delta \hat{X}_1^2 \rangle$ and $\langle \Delta \hat{X}_2^2 \rangle$ (*23*). The extracted bath occupations are plotted in Fig. 3C, and the quadrature variances are shown in Fig. 3D. We find that, at our lowest point, we are squeezed to $0.80 \pm 0.03\ x_{zp}^2$, or 1.0 ± 0.2 dB below the zero-point fluctuations. The spectral fit for this point is shown in Fig. 3B.

To directly measure the fluctuations of a single quadrature, it is possible to introduce a set of weak back-action evading tones in addition to the squeezing tones (*24*) (Fig. 4A). This type of back-action evading measurement has the advantage that thermal cavity noise does not affect the measured fluctuations. In order for the presence of the probe tones not to interfere with the measured mechanical quadrature, the probe sideband must be separated from the squeezing sideband by many mechanical linewidths. For this device, where the mechanical linewidth at optimal squeezing is ~15% of the cavity linewidth, such a separation would place the probe sideband outside the cavity bandwidth, appreciably decreasing the probe gain and leading to unrealistic measurement times. However, we have implemented such a measurement scheme using a similar device with a larger cavity bandwidth, $\kappa = 2\pi \times 860$ kHz, and narrower mechanical linewidth, $\gamma_{tot} = 2\pi \times 10$ kHz (Fig. 4B). As is shown in Fig. 4C, the phase-dependent BAE measurement shows the expected squeezed thermal state produced by the two squeezing pumps, with minimum fluctuations of $1.09 \pm 0.06\ x_{zp}^2$, limited in a similar way as the first device by heating. This measurement demonstrates the quadrature squeezing produced by imbalanced pumps at $\omega_c \pm \omega_m$, as described by the theory.

Although a squeezed thermal state always has a positive Wigner function, when the fluctuations in one quadrature are reduced below the zero-point level, the squeezed state no longer has a well-behaved P representation—that is, it cannot be represented as an incoherent mixture of coherent states (*25*). For this reason, a quantum squeezed state is considered a nonclassical state. It is a current goal to study the nonclassical behavior in larger and larger systems, and recent progress in the field of opto- and electromechanics has resulted in the generation of mechanical Fock states (*26*), entanglement between photons and phonons (*27*), and observation of the mechanical zero-point fluctuations (*28*); quantum squeezing in a micrometer-scale mechanical resonator is an important addition to this list.

REFERENCES AND NOTES

1. R. E. Slusher, L. W. Hollberg, B. Yurke, J. C. Mertz, J. F. Valley, *Phys. Rev. Lett.* **55**, 2409–2412 (1985).
2. B. Yurke *et al.*, *Phys. Rev. Lett.* **60**, 764–767 (1988).
3. D. M. Meekhof, C. Monroe, B. E. King, W. M. Itano, D. J. Wineland, *Phys. Rev. Lett.* **76**, 1796–1799 (1996).
4. J. Hald, J. L. Sørensen, C. Schori, E. S. Polzik, *Phys. Rev. Lett.* **83**, 1319–1322 (1999).
5. T. J. Dunn, J. N. Sweetser, I. A. Walmsley, C. Radzewicz, *Phys. Rev. Lett.* **70**, 3388–3391 (1993).
6. G. A. Garrett, A. G. Rojo, A. K. Sood, J. F. Whitaker, R. Merlin, *Science* **275**, 1638–1640 (1997).
7. A. Kronwald, F. Marquardt, A. A. Clerk, *Phys. Rev. A* **88**, 063833 (2013).
8. D. Kienzler *et al.*, *Science* **347**, 53–56 (2015).
9. D. Rugar, P. Grütter, *Phys. Rev. Lett.* **67**, 699–702 (1991).
10. P. Rabl, A. Shnirman, P. Zoller, *Phys. Rev. B* **70**, 205304 (2004).
11. R. Ruskov, K. C. Schwab, A. N. Korotkov, *Phys. Rev. B* **71**, 235407 (2005).
12. K. Jähne *et al.*, *Phys. Rev. A* **79**, 063819 (2009).
13. M. R. Vanner *et al.*, *Proc. Natl. Acad. Sci. U.S.A.* **108**, 16182–16187 (2011).
14. A. Szorkovszky, G. A. Brawley, A. C. Doherty, W. P. Bowen, *Phys. Rev. Lett.* **110**, 184301 (2013).
15. A. Vinante, P. Falferi, *Phys. Rev. Lett.* **111**, 207203 (2013).
16. A. Pontin *et al.*, *Phys. Rev. Lett.* **112**, 023601 (2014).
17. J. I. Cirac, A. S. Parkins, R. Blatt, P. Zoller, *Phys. Rev. Lett.* **70**, 556–559 (1993).
18. V. B. Braginsky, Y. I. Vorontsov, K. S. Thorne, *Science* **209**, 547–557 (1980).
19. F. Marquardt, J. P. Chen, A. A. Clerk, S. M. Girvin, *Phys. Rev. Lett.* **99**, 093902 (2007).
20. J. Gao *et al.*, *Appl. Phys. Lett.* **92**, 152505 (2008).
21. J. Suh, A. J. Weinstein, K. C. Schwab, *Appl. Phys. Lett.* **103**, 052604 (2013).
22. J. D. Teufel *et al.*, *Nature* **475**, 359–363 (2011).
23. Materials and methods are available as supplementary materials on *Science* Online.
24. J. Suh *et al.*, *Science* **344**, 1262–1265 (2014).
25. M. S. Kim, F. A. M. de Oliveira, P. L. Knight, *Phys. Rev. A* **40**, 2494–2503 (1989).
26. A. D. O'Connell *et al.*, *Nature* **464**, 697–703 (2010).
27. T. A. Palomaki, J. D. Teufel, R. W. Simmonds, K. W. Lehnert, *Science* **342**, 710–713 (2013).
28. F. Lecocq, J. D. Teufel, J. Aumentado, R. W. Simmonds, *Nat. Phys.* **11**, 635–639 (2015).

ACKNOWLEDGMENTS

This work is supported by funding provided by the Institute for Quantum Information and Matter, an NSF Physics Frontiers Center with support of the Gordon and Betty Moore Foundation (NSF-IQIM 1125565), by the Defense Advanced Research Projects Agency (DARPA-QUANTUM HR0011-10-1-0066), by the NSF (NSF-DMR 1052647 and NSF-EEC 0832819), and by the Semiconductor Research Corporation (SRC) and Defense Advanced Research Project Agency (DARPA) through STARnet Center for Function Accelerated nanoMaterial Engineering (FAME). A.A.C., F.M., and A.K. acknowledge support from the DARPA ORCHID program through a grant from AFOSR, F.M. and A.K. from ITN cQOM and the ERC OPTOMECH, and A.A.C. from NSERC.

SUPPLEMENTARY MATERIALS

www.sciencemag.org/content/349/6251/952/suppl/DC1
Materials and Methods
Figs. S1 to S5
References (*29*–*32*)

7 May 2015; accepted 28 July 2015
10.1126/science.aac5138

Editor's Summary

Manipulation of a quantum squeeze

The uncertainty principle of quantum mechanics dictates that even when a system is cooled to its ground state, there are still fluctuations. This zero-point motion is unavoidable but can be manipulated. Wollman *et al.* demonstrate such manipulation with the motion of a micrometer-sized mechanical system. By driving up the fluctuations in one of the variables of the system, they are able to squeeze the other related variable below the expected zero-point limit. Quantum squeezing will be important for realizing ultrasensitive sensors and detectors.

Science, this issue p. 952